2212-

Mapping MMS Observations of Solitary Waves in Earth's Magnetic Field

P. J. Hansel[1], F. D. Wilder[1,2], D.M. Malaspina[1,3], R. E. Ergun[1,3], N. Ahmadi[1], J.C. Holmes[11], K. A. Goodrich[6], S. Fuselier[7], B. Giles[3], C. T. Russell[8], R. Torbert[9], R. Strangeway[8], Y. Khotyaintsev[5], P.-A. Lindqvist[10], J. Burch [7]

[1]Laboratory for Atmospheric and Space Physics, 1234 Innovation Drive, Boulder CO 80303, USA
[2]University of Texas, Arlington
[3]Astrophysical and Planetary Sciences Department, University of Colorado, Boulder, CO
[4]Goddard Spaceflight Center
[5]Swedish Institute of Space Physics, Uppsala, Sweden
[6]University of California, Berkeley
[7]Southwest Research Institute, Boulder, Colorado
[8]University of California, Los Angeles
[9]Space Science Center, University of New Hampshire
[10]KTH Royal Institute of Technology
[11]Space Research Institute, Austrian Academy of Sciences

Key Points:

- The MMS Solitary Wave Detector records time-domain structures in Earth's magnetosphere
- SWD maps highlight regions like the Van Allen belts and the bursty bulk flow braking region
- The SWD shows intriguing nonlinear activity in the shocks, magnetotail, flank, and dawn-side outer radiation belt

Corresponding author: Paul Hansel, paul.hansel@colorado.edu

Abstract

Electrostatic solitary waves (ESWs) are a type of nonlinear time-domain plasma structure (TDS) generally defined by bipolar electric fields and propagation parallel to the local magnetic field. Formation mechanisms for TDSs in the magnetosphere have been studied extensively and are associated with plasma boundary layers and the braking of bursty bulk flows (BBFs). However, the rapid timescales over which these TDSs occur (<2 ms) make them infeasible to count by eye over large time periods. Furthermore, high-cadence data are not always available. The Solitary Wave Detector (SWD) on NASAs Magnetospheric Multiscale (MMS) mission quantifies the occurrence and amplitude of TDS throughout the constellations orbit; analysis of burst (65 kS/s) parallel electric field data indicates that the SWD captures appx. 60% of all bipolar TDS encountered in the tail region, enabling large-scale examination of their occurrence. Maps of TDS occurrence rates during several years of the MMS mission were generated from SWD data, showing enhanced TDS density in the tail region between 6-9 Re; enhance occurrence in or near shocks; and an unexpected enhancement in the dawn side of the tail and in the radiation belt.

1 Introduction

Kinetic instabilities are important for understanding the mediation of energy between particles and electromagnetic fields in space plasmas. Time Domain Structures (TDS) are an important subset of electric field structures associated with the non-linear evolution of these kinetic instabilities. TDS are typified by short time-duration pulses in the electric field component parallel to the background magnetic field, E$\|$, and have broadband frequency spectra (Temerin et al., 1982; Matsumoto et al., 1994; Ergun et al., 1998). TDS have been speculated to be important for particle acceleration processes in the Earths magnetosphere (F. S. Mozer et al., 2016). They can include unipolar electric field signatures that are associated with an electrostatic potential drop, known as double layers, as well as bipolar electric field signatures, called electrostatic solitary waves (ESWs). (Vasko et al., 2017) ESWs can correspond to a variety of plasma structures, including electron phase-space holes (Muschietti et al., 1999), ion phase-space holes(Main et al., 2006), electron bunching associated with non-linear wave evolution (Wilder et al., 2016), and structures resulting from plasma mixing (Holmes et al., 2018). TDS and ESWs have been observed in several regions of geospace, including the auroral acceleration region (Ergun et al., 2002; Andersson et al., 2002), the dayside magnetopause (Cattell et al., 2002), the bursty bulk flow (BBF) braking region of the Earths magnetotail (Ergun et al., 2015), the Earths bow shock (Goodrich et al., 2018), and the solar wind upstream of Earth (Mangeney et al., 1999; Malaspina et al., 2013).

One example of TDSs that are important to understanding the magnetosphere is the fast Earthward flows resulting from magnetic reconnection in the magnetotail. These flows decelerate as they approach Earth and are diverted around the ring current. This braking occurs on the nightside, skewed towards the dusk, between 6 and 10 Re away from Earth (Sergeev et al., 2009; Ergun et al., 2015; McPherron et al., 2011). As these flows decelerate, their associated kinetic energy is deposited into the local plasma population, leading to a turbulent cascade (Stawarz et al., 2015). One significant question is how that turbulent cascade is dissipated on the kinetic scales. Ergun et al. (2015) and Zhang et al. (2020) reported the presence of double layers in the flow-braking region, which can act to dissipate small-scale currents in turbulence. A clear signature of these double layers is a train of electron phase-space holes. One challenge in studying the characteristics of electron phase space holes and other ESWs in the BBF braking region is the fact that they correspond to structures on the order of a few Debye lengths. These structures consequently require high-resolution electric field measurements in order to be studied.

Another example in which TDSs can play an important role is at shocks. Localized ion-acoustic waves and other nonlinear, localized wave events have long been associated with shocks and may play a role in thermalizing the heated electron and ion distributions (e.g. Formisano & Torbert, 1982; Fuselier & Gurnett, 1984; Wilson et al., 2014; Goodrich et al., 2018). TDSs are also seen along the separatrix of magnetic reconnection (e.g. Wilder et al. (2016)). Nonlinear kinetic structures are an important indicator of substantial energy exchange or dissipation.

In 2015, NASA launched the Magnetospheric Multi-scale (MMS) mission in order to study the phenomenon of magnetic reconnection in Earths magnetosphere, with an instrument suite optimized for the study of kinetic plasma physics. The MMS suite includes six electric field double probes: the Spin-plane Double Probes (SDP) are 120 m tip-to-tip in the spin plane (Lindqvist et al., 2016) and the Axial Double Probes (ADP) extend 15 m from each side of the spacecraft along the axis of rotation (Ergun et al., 2016). Together, the SDP and ADP capture the 3-D electric field. The EDP burst data mode includes DC-coupled electric fields measured at a configurable rate up to 16,384 samples/s and AC coupled fields measured at up to 262,144 S/s. Burst-mode data also includes electron and ion distributions and moments measured by the Fast Plasma Investigations (FPI) at 30 ms and 150 ms cadence, respectively(Pollock et al., 2016). The high-cadence burst data is ideal for investigating TDS events. However, high-cadence burst is available for less than 4% of an MMS orbit on average. The advantage MMS has for the study of ESWs and TDSs is an onboard, always-on Solitary Wave Detector (SWD). This algorithm operates in each spacecrafts digital signal processing (DSP) board and searches the burst data from the spin-plane electric double probes (SDP) for non-linear spiky wave structures (Ergun et al., 2016). Specifically, SWD examines only signals from the first set of opposing spin-plane probes (V1-V2) by default and uses V3-V4 as a fallback. The SWD algorithm reports the number of TDS events detected in a given amplitude range as a histogram. In addition to studying individual wave events in the burst, MMS therefore provides the capability to study ESWs in a statistical manner, since SWD data is available throughout the entire orbit and not restricted to burst data periods.

In the present study, we investigate the incidence of time domain structures in the Earths magnetosphere with a focus on the near-Earth magnetotail. During intervals where burst electric field data is available in the magnetotail, we compare the SWD data with the actual observations of ESWs by the EDP instrument. We find that the SWD detects approximately 60% of solitary waves observed in the tail (Table 1). We then generate statistical maps of SWD counts, observing TDS occurrence throughout the Earths magnetosphere. Additionally, we find that the SWD captures many of the boundaries in the Earths magnetosphere, including the bow shock, radiation belts, magnetopause, and possibly even the BBF braking region. This suggests that algorithms like the SWD can be useful in large-scale studies of magnetospheric activity.

2 Solitary Wave Detector Algorithm

The MMS DSP SWD algorithm operates in real-time aboard each MMS spacecraft. The DSP analog-to-digital converters take capacitively coupled voltages from the V1-V2 spin-plane electric double probes (EDP) as inputs. A 1/256th second sliding window is used to test for the presence of TDS; within the SWD algorithm, EDP data is downsampled from 262,144 S/s to 65,536 kS/s and its average value over a single 256-point window's width is removed. A pseudo-RMS value is then determined for each unique window as follows (Ergun et al., 2016):

$$pRMS = \frac{1}{n}\sum_{i=0}^{n-1}|E12_i| \quad (1)$$

where n is the number of samples per window and $E12_i$ is the ith measured parallel electric field value between spin-plane probes 1 and 2. Bin voltage thresholds were precomputed and stored in the DSP (Ergun et al., 2016).

The peak value of $|V|$ within the window is divided by the pRMS to determine the number of pseudo-standard deviations of the peak. If this value is above a configurable constant (currently 4), the event is determined to be a solitary wave or nonlinear structure and one of four counters is incremented (Ergun et al., 2016). Each second, these counters are recorded and reset. Four event counters are used to register the peak amplitudes of the event. The four counters represent, approximately, 0.3 to 3 mV/m, 3 to 12 mV/m, and >50 mV/m. The instrument saturates at 333 mV/m.

In short, the SWD selects peaks in 4 ms periods that are 4 pseudo-standard deviations above background, which corresponds to approximately 3.58 standard deviations (true RMS). Under a purely random sequence of sufficient amplitudes, the SWD selects one event every 5000 seconds (background).

3 SWD Case Study and Validation

This case study occurs between 2016-08-09/09:00:00-10:00:00 UTC. An overview of the event can be found in Figure 1.

TDS Amplitude Bin	Absolute N	Intercept	Slope	r	r^2	StdErr
3 - 12 mV/m	28299	0.3784	0.6125	0.699	0.487	0.005
12 - 50 mV/m	7354	0.0981	0.6206	0.720	0.518	0.005
50+ mV/m	322	0.0076	0.5932	0.599	0.359	0.007

Table 1: Regression parameters for efficacy of MMS SWD bins 2, 3, 4 as gauged by relative measurement accuracy against ground algorithm (MMS1,2,3,4 2016-08-09 09:00:00 - 10:00:00 UTC)

The key assumption behind the SWD is that the presence of time-domain structures (TDS) - electron holes or otherwise - can be deduced from one component of the electric field at a high enough sample rate. With only one axis of measurement per spacecraft, however, some fraction of TDS events will be missed, particularly those with low-amplitude. By contrast, high-amplitude ESW as observed in Goodrich et al. (2018) are rare and visually distinct (Figure 1, near 2016-08-09 09:20:00 UTC). Furthermore, two closely-spaced bipolar structures may raise the RMS background so that neither of the events are detected. The challenge in gathering useful statistics about TDS is to accurately detect and count lower-amplitude TDS.

3.1 MMS SWD Calibration and Interpretation

Bipolar electric field structures are known to be abundant in the near magnetotail, so we characterize how well the SWD detect these structures so that the SWD data can be better interpreted. We compare the SWD with selections from AC-coupled burst data recorded from the 1-2 spin plane electric double probes (EDP) shown in Figure 1(f). A more

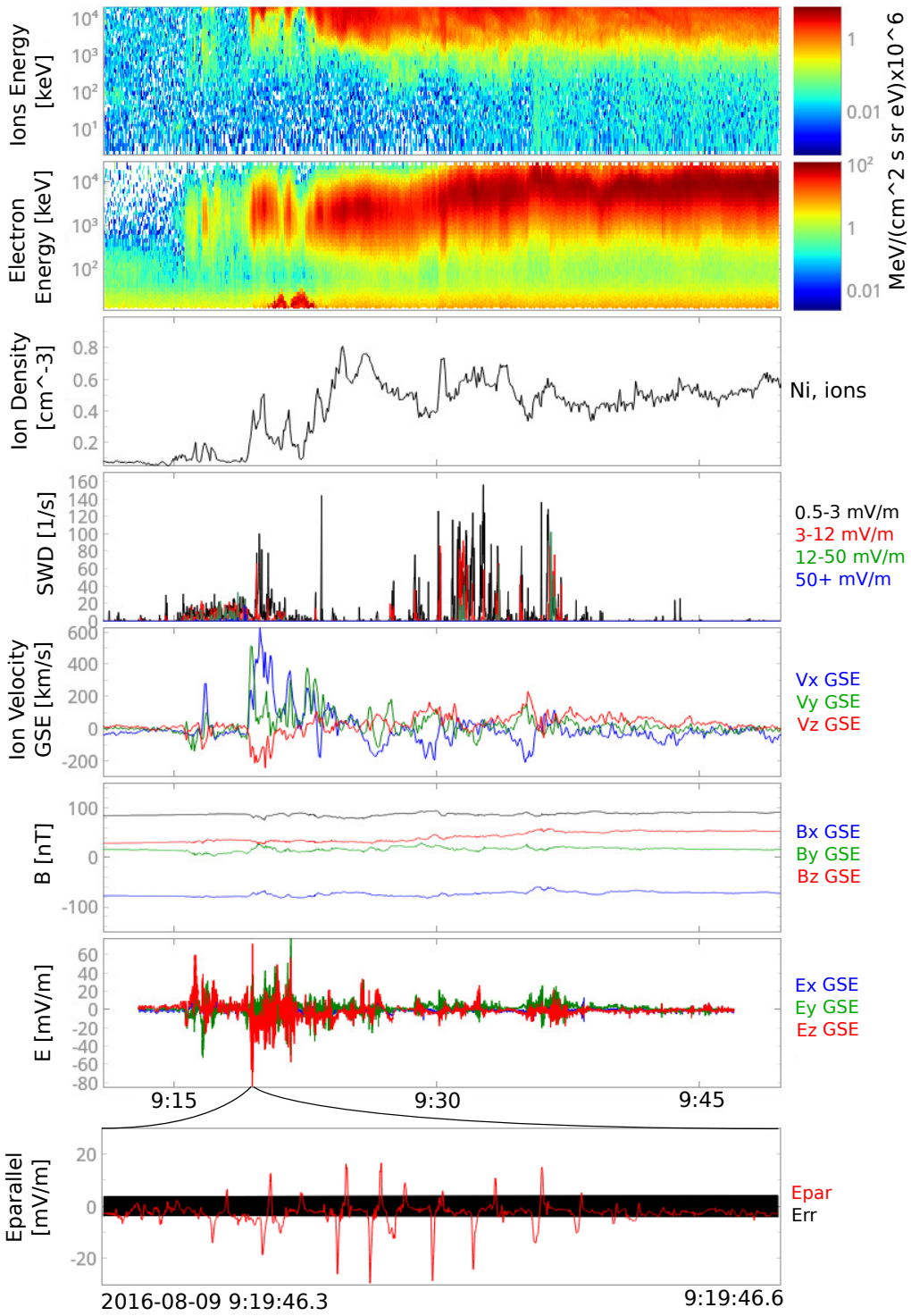

Figure 1: Case study plot for bursty bulk flow braking event in Earth near-tail; (a) electron energy spectra; (b) ion energy spectra; (c) ion density; (d) DSP SWD counts; (e) ion bulk velocity; (f) GSE electric field; (g) GSE magnetic field; and (h) zoomed segment of E-parallel, showing individual ESWs. MMS1 data from 2016-08-09 09:00-9:45 UTC. From the Bx (GSE) component of the magnetic field, the MMS spacecraft was in the southern lobe. At around 9:20 UT, the Bx-component magnitude decreases, as the Vx (GSE) component turns strongly northward, with a magnitude exceeding 600 km/s. Further, after the flow enhancement there is an increase in plasma density. All of these are signatures of a bursty bulk flow (BBF) (Sergeev et al., 2009). BBFs are a phenomena where ESWs can be observed (Ergun et al., 2015) and are thus ideal to evaluate the performance of the SWD.

sophisticated algorithm acting on high-cadence data is used to segment solitary waves and characterize them by rescaling to fit a prototypical bipolar waveform, or kernel. A description of this ground algorithm is located in Appendix A. The observation period for this characterization is 2016-08-09 from 9:00-10:00 UTC, the same data displayed in Figure 1. During this time period, MMS was in the near tail circa GSE X = -7.7, Y = 3.2, Z = 0.44. This characterization is primarily relevant to observations in the tail (e.g. the BBF braking region) and less applicable where ion-acoustic waves are more active, such as the bow shock (Goodrich et al., 2018).

A linear fit of SWD against ground TDS detector counts for the highest three bins (2-4) is described in Table 1, and plots showing data and regression lines for each bin are found in Figure 2. In these regressions, the abscissa is the ground algorithm count; the ordinate is the count rate provided by DSP SWD.

The correlation coefficients of these regressions are in the range of 0.59 - 0.62; for every bipolar event present per second (as established by the ground TDS algorithm), the SWD registers approximately 0.6 events per second. Variance in TDS counts only explain 35-51% of the variance in SWD counts for the two highest bins. Particularly at high bipolar event densities, the SWD tends to underestimate occurrence rates; if other non-ESW-like structures are present, e.g. Whistler waves, which still fulfil the SWD requirement of a high peak-to-pRMS ratio, the SWD count can be inflated. Such non-bipolar events may explain the unusually high expected Bin 2 count rate of 0.3784 given zero TDS.

Another possible mechanism for variance in the SWD is erroneous binning, where superposed structures artificially increase peak-to-peak values or digital filtering flattens them, causing detected structures to be placed in too high or too low a bin. To reduce the error caused by this effect, the ground detector assigns amplitude bins using the average peak amplitude for each TDS rather than the maximum absolute value.

The MMS SWD algorithm allows TDS occurrence rates and amplitudes to be logged over full orbits of the MMS constellation.(Ergun et al., 2016) Previous studies have characterized limited numbers of ESWs by velocity, temporal duration, potential, length, etc. In general, ESWs have been detected by the Geotail and THEMIS spacecraft with velocities between 6,000-38,000 km/s, temporal durations between 0.5-20 milliseconds, lengths circa 1 λ_D, and potential depths of 1.3-270 V. (Omura et al., 1999) Physical scales of ESWs and BBFs tend to scale with Debye length, which decreases as $|B|$ increases, e.g. at distances closer to Earth; consequently, ESWs far from Earth or in the far tail (>80 Re) are typically larger than those closer to the Earth (Omura et al., 1999) .

Pulse trains of ESWs with smaller amplitudes (~100 $\mu V/m$) have been observed in the far tail (circa GSM X = -120 Re) as reported in other research (Kojima et al., 1999). From 2015-2020, MMS' apogee over Earth remained within 30 Re or less, and the minimum threshold necessary to trigger the SWD corresponded to an amplitude of 0.5 mV/m. During observation periods near the dayside magnetopause, when the MMS spacecraft are in close formation (<10 km separation), the same patterns of solitary waves have been seen on multiple satellites (Holmes et al., 2018). Large ranges in length scales and speeds have been observed (Graham et al., 2016), on the order of 10-20 λ_D and 3000-10000 km/s respectively (F. S. Mozer et al., 2016). The scope of this case study is thus limited to the particular regime between 1.5-30 Re in GSE X and Y and -6 to +6 in GSM Z where time domain structures of interest exceed amplitudes of 0.5-3 mV/m.

3.2 Spatial Map Observations

In the previous subsection, we have shown that the SWD can detect approximately 60% of bipolar events in the Earth's magnetotail, enabling its use in statistical studies. Since

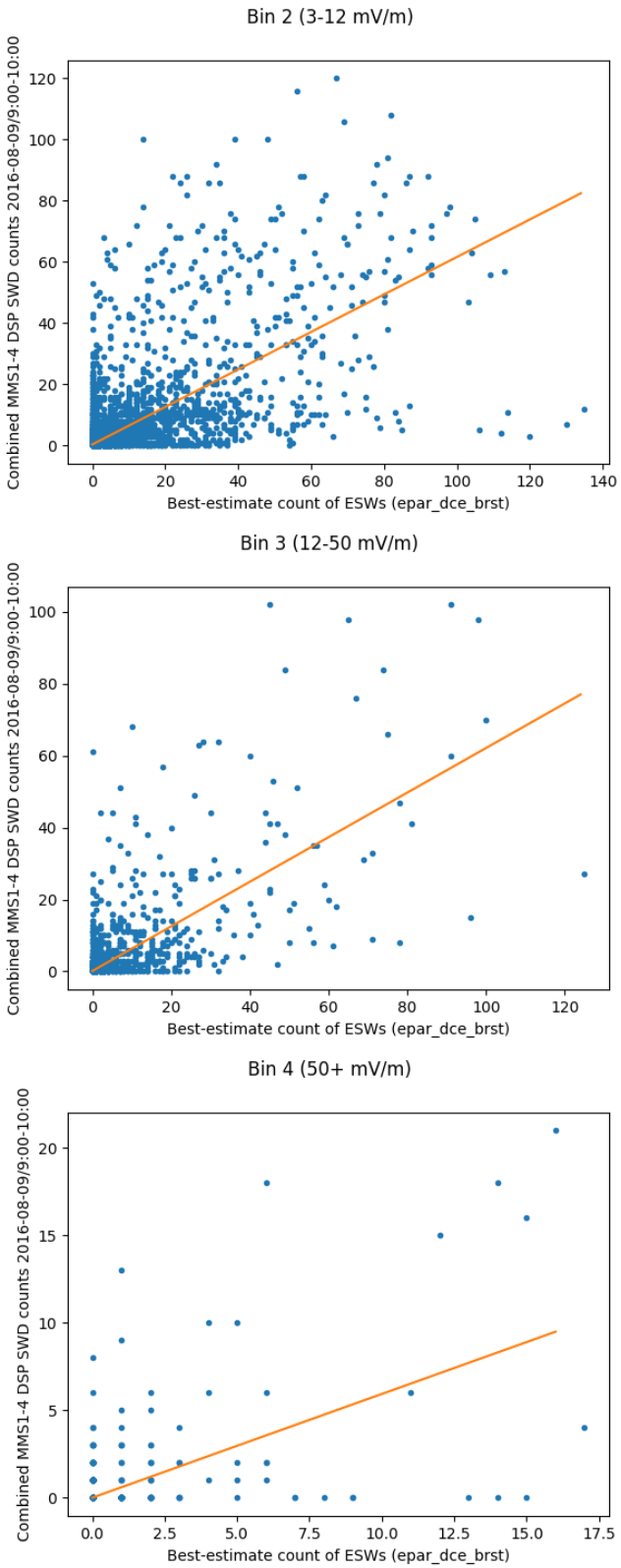

Figure 2: Case study of DSP SWD counts (Bins 2, 3, 4) plotted against ground algorithm bipolar event counts (blue) with best-fit regression lines (orange)

the SWD is the first algorithm of its kind on a spacecraft, it is valuable to map out the counts through the duration of the mission so as to determine an average representation of conditions in the magnetosphere. We thus generate maps (Figures 3-4) using data from all four MMS spacecraft starting in August 2015 (shortly after launch) through March 2020. This encompasses a broad range of magnetospheric history and space; the MMS spacecraft surveyed nearly all points within a radius of 30 Re from Earth defined by our rectangular grid scale of 1 Re. Most of the characteristic features of Earth's magnetosphere are present in the SWD maps: the bow shock, magnetosheath, and one or both of the Van Allen belts are visible. The bow shock visible in SWD maps can be compared to the bow shock clearly denoted by the ion bulk velocity discontinuity (rapid divergence from solar wind bulk velocity, Figure 5) and the ion density gradient (sharp increase in ion density, Figure 6), all shown with a plotted average bow shock and magnetopause. In SWD maps, the bow shock signature extends farther into the solar wind than the statistical shock or either boundaries shown by ion data. By comparison, the magnetopause boundary appears absent from the SWD maps, while it is clearly visible in ion density (sharp density decrease, corresponding to Earth's near-vacuum plasmasphere) and bulk velocity (gradual reversal of flows in the +X direction). A different gradient is visible in SWD maps, closer to the midline of the magnetosheath.

Based on past statistical studies showing tailward BBFs are more prominent on the dusk (+Y) side of the magnetotail, while Earthward flows are nearly symmetrically distributed or slightly more prominent on the dusk side (Kiehas et al., 2018), it is an unexpected result that the SWD counts are concentrated on the dawn (-Y) side. ARTEMIS studies in the midtail magnetosheath have shown substantially higher fluxes for hot electron enhancements on the dawn side versus the dusk side, which could explain this asymmetry (Wang et al., 2015).

Figure 4 shows that the average for 3-12 mV/m solitary waves in the magnetosheath is approximately 1.5/s per spacecraft. Within the solar wind, and towards the magnetotail, the average is approximately 0.001/s, or one TDS every 1000 seconds. The largest observed average value, of around 250/s in bin 1, highlights the instrument's maximum counting capability of 256/s; a maximum of 10-50/s in bins 2-3 is seen around the bow shock and magnetopause.

As seen in Figure 1, TDS with amplitudes >50 mV/m are relatively rare, contributing to the sparseness of maps of higher amplitude bins (Figure 4, bottom). For the maps of 50+ mV/m TDS, all spatial bins have averages lower than $10^{-4.5}/s$, corresponding to an average period of approximately 9 hours between individual detection events. By contrast, the high counts in the bow shock could include various ESW and non-ESW time-domain structures such as double layers and non-linear acoustic wave bursts (Goodrich et al., 2018).

Similar gradients in count rates across the magnetopause, bow shock, and solar wind are present in all amplitude bins. The spatial resolution of these maps is limited by sample density and dynamic range (i.e. number of amplitude bins), but some key differences between the maps are present. For example, a hot spot near GSM X,Y = (-3,-4) Re appears sharpest in the 12-50 mV/m amplitude range (Bin 3) as compared to bins 1, 2, or 4, while the Van Allen belt ring structure at 2-3 Re appears much more continuous in Bin 1 than Bins 2-4. The overall BBF braking region SWD enhancement, by contrast, is approximately the same size (15 Re across) across all bins. Interestingly, the map of 12 to 50 mV/m TDS (Figure 4, top) has a visible peak in the dawn-side radiation belt at L = 4. The character of the events cannot be examined for this unexpected peak since MMS does not acquire burst data inside 7 Re.

These maps indicate that some TDS are present within the solar wind but not at a significant level (less than one per 10^7 seconds). This finding is consistent with WIND observations in the solar wind (Malaspina et al., 2013).

4 Conclusions

The primary goal of the Magnetospheric Multiscale Mission is to improve our understanding of magnetic reconnection and the distribution of energy across multiple scale regimes in Earth's magnetosphere. The Solitary Wave Detector aboard MMS is a unique algorithm that provides complex data about electric field phenomena relative to its hardware cost and downlink impact.

Through a statistical study of typical SWD and parallel electric field data, we find that the SWD performs as intended; namely, it observes electron phase-space holes and detects structures associated with magnetic reconnection (Ergun et al., 2016). We found that SWD counts are approximately 60% correlated with TDS detectable via ground software on the spin-plane electric double probes. However, with none of the amplitude levels' r-squared values exceeding 0.518, only around 45% of the variance in SWD is explained by actual TDS occurrence.

It is difficult to determine the exact nature of events observed by SWD, because the algorithm does not differentiate between different types of plasma structures. Nonetheless, it correctly and consistently identifies large excursions in the electric field. For a scientist-in-the-loop (SITL) whose task is to select which segments of high-fidelity data should be downlinked, enhancement in SWD counts can highlight plasma activity like dipolarization fronts and bursty bulk flows (Le Contel et al., 2017), which can inform potentially novel observations that may be more difficult to see in survey data.

The SWD algorithm also presents information in a simple format that is amenable to visualization. Within spatial maps of average SWD counts, one can perceive basic features of Earth's magnetosphere: the bow shock, magnetopause, and van Allen belts. Each feature has a recognizable signature and is essentially spatially consistent with our understanding of Earth's magnetospheric system. Filtering by amplitude bin enhances the visibility of certain regions and reduces the visibility of others, showing spatial differences in energetic ESW evolution. Moreover, compiling multi-year observations from MMS can bring previously unobserved large-scale asymmetries and gradients into view. Through a four-year mapping of data from MMS, we show various important features of the magnetosphere as illuminated by the SWD.

At Earth's bow shock, the SWD can pick up a variety of nonlinear plasma structures including solitary waves, double layers, and nonlinear ion-acoustic wave packets that are bursty in nature (Goodrich et al., 2018, 2019). At the magnetopause, magnetic reconnection is a potential source for solitary waves by producing unstable electron distributions and/or strong currents (Graham et al., 2016). Both the bow shock and magnetopause are visible in maps of SWD data.

One striking result is how well the SWD captures the Van Allen belts. F. Mozer et al. (2013) suggested that TDS, including double layers and ESWs, are important for the dynamics of the Van Allen belts, and the present study confirms that these structures are ubiquitous in that region (Figures 3-4). Past (and present) research has used transitions in data revealed by new instruments to perform statistical analyses of the regions and dynamics giving rise to those transitions (Neugebauer & Snyder, 1962); that the SWD consistently marks the location of magnetospheric phenomena suggests that it is also possible to perform more detailed statistical studies of SWD counts in various regions.

Substorm models of magnetospheric activity have typically included bulk flows (BF) toward the Earth resulting from energy released during tail magnetic reconnection (Sergeev et al., 2009). SWD maps show a clear enhancement in TDS density in this tailward 6-9 Re region.

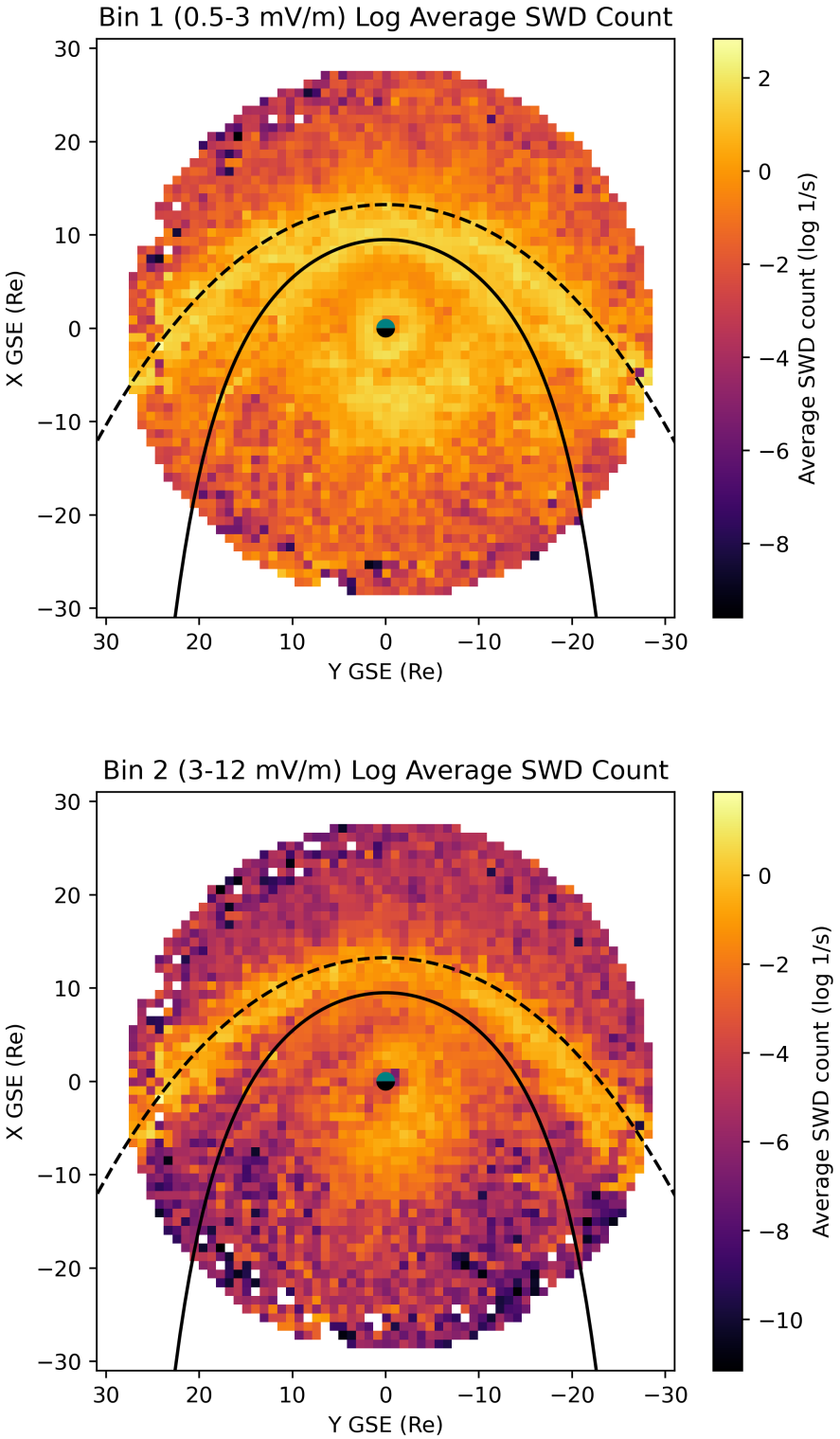

Figure 3: Composite maps from MMS 1-4 of log mean SWD count rates (Bins 1-2) within GSM X-Y plane between August 2015 and April 2020; statistical bow shock (dashed), magnetopause (solid) and Earth (blue/black) shown.

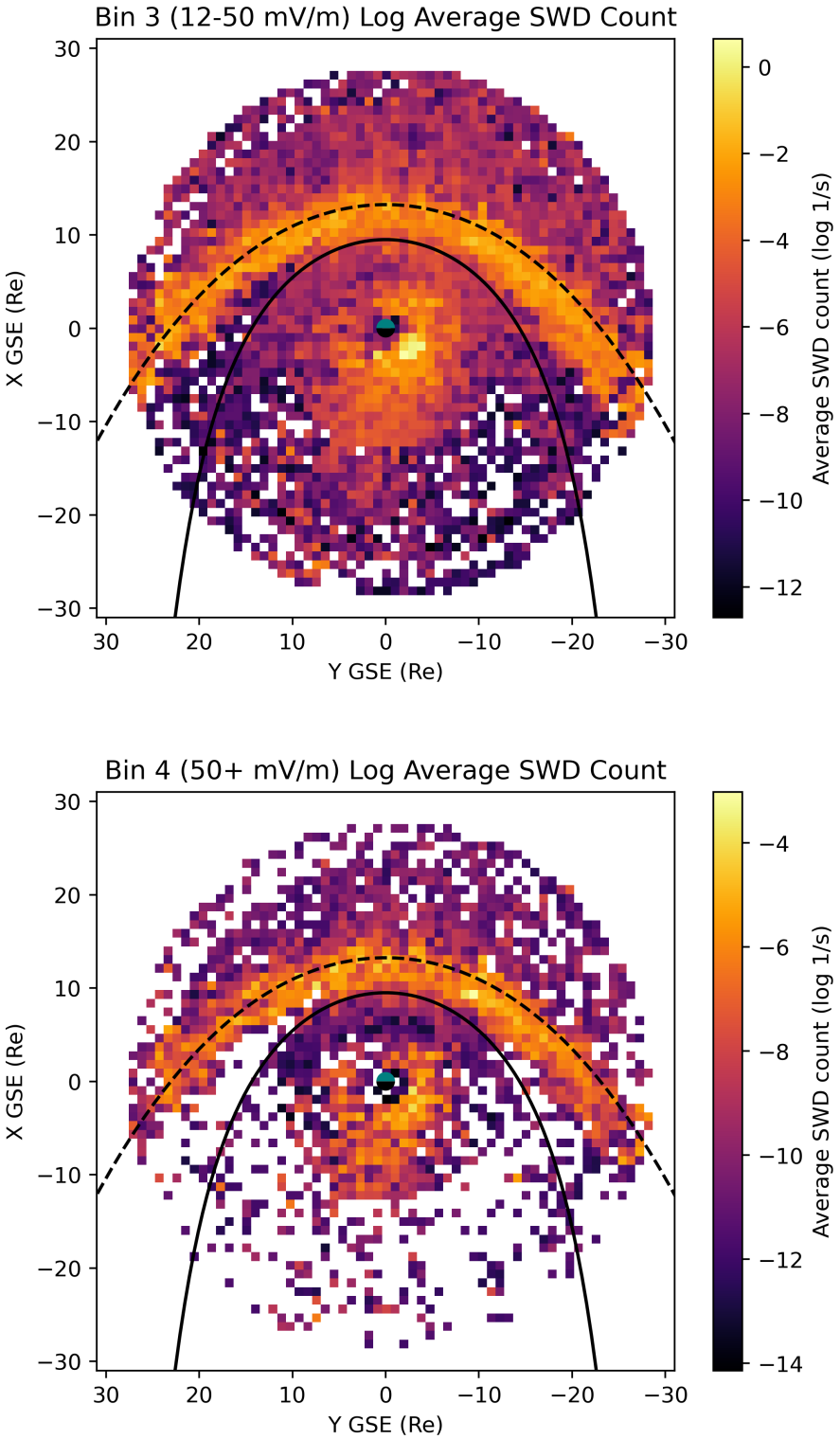

Figure 4: Composite maps from MMS 1-4 of log mean SWD count rates (Bins 3-4) within GSM X-Y plane between August 2015 and April 2020; statistical bow shock (dashed), magnetopause (solid) and Earth (blue/black) shown.

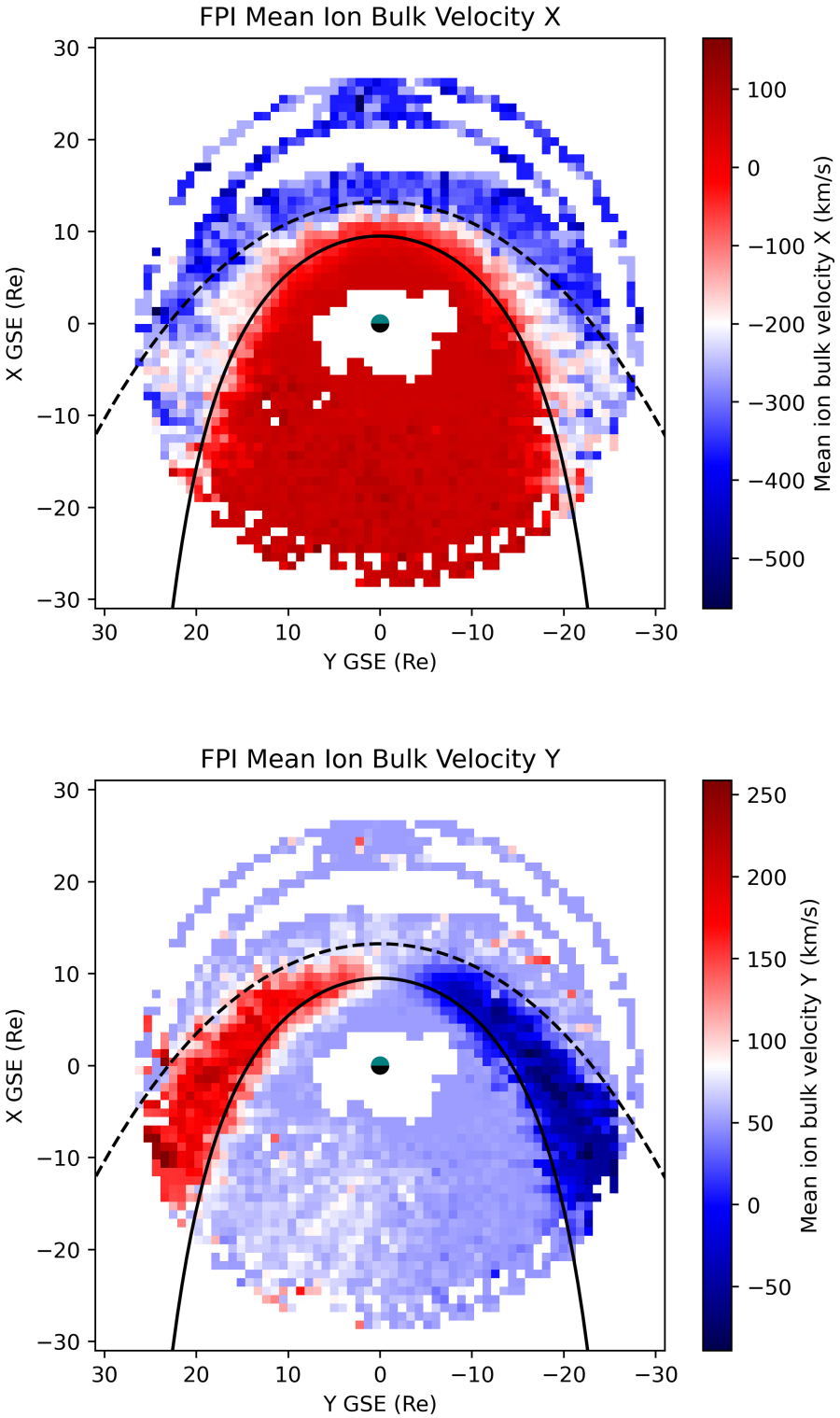

Figure 5: FPI ion bulk velocity along GSE X (top) and Y (bottom) vectors; statistical bow shock (dashed), magnetopause (solid) and Earth (blue/black) shown. Data gathered between August 2015 and April 2020.

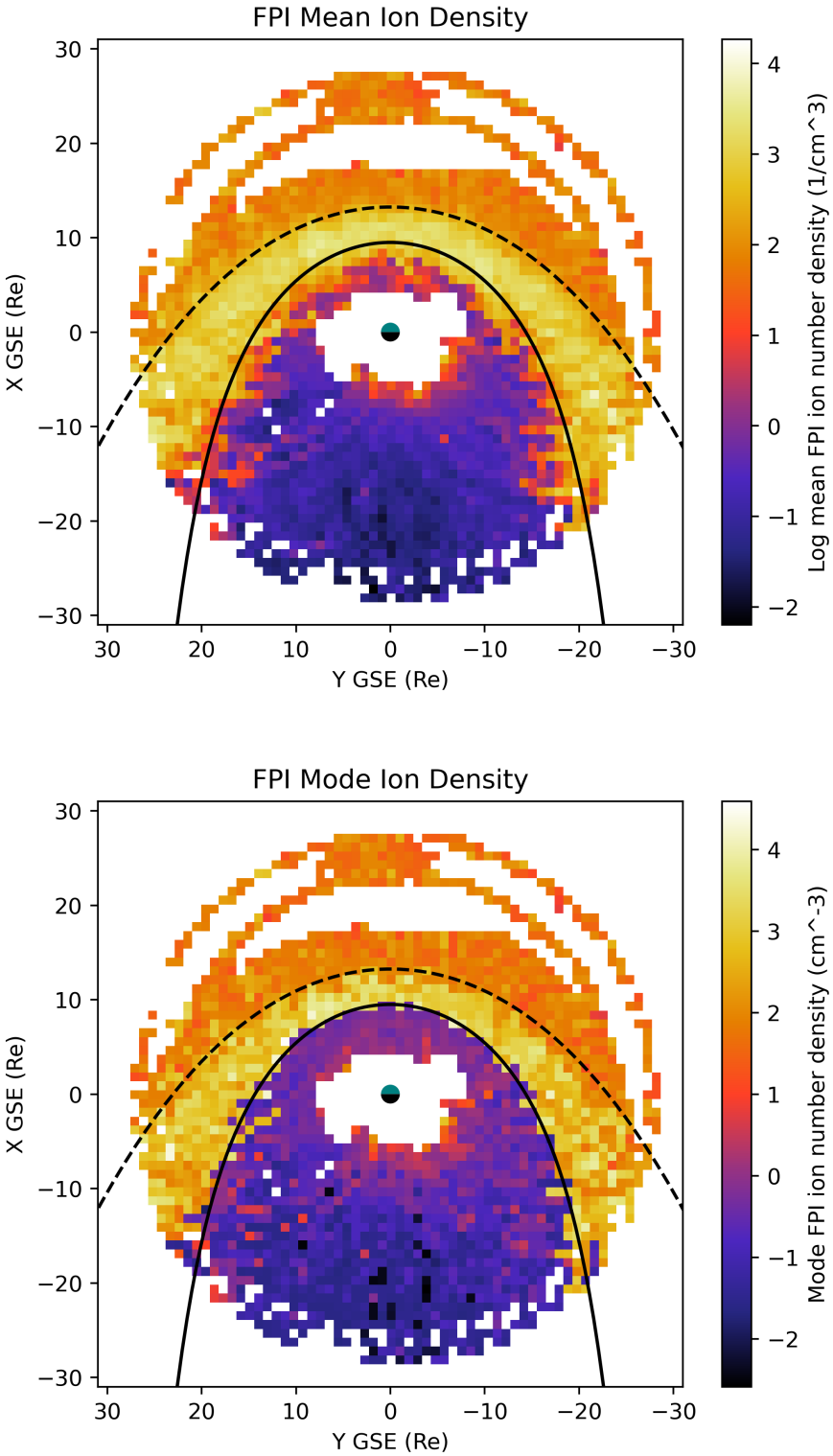

Figure 6: Average (top) and typical (bottom) ion number density; statistical bow shock (dashed) and magnetopause (solid) and Earth (blue/black) shown. Data gathered between August 2015 and April 2020.

Most surprisingly, the dawn-dusk braking region is asymmetrically biased towards the dawn side of Earth; this is an unexpected and important result. This asymmetry is present in maps from bins 1-4, corresponding to all amplitudes of TDS >0.5 mV/m observed by MMS SWD. A hot spot within this region is visible around X = -2 Re, Y = -3 Re (Figure 4, top); given that these observations are mostly independent of Earth's rotation, this feature may be fixed with respect to the solar wind and not some structure of Earth's magnetic field fixed to the surface (e.g. the South Atlantic Anomaly). A slight asymmetry in bulk GSE Y velocity is also visible on the dusk tail of Earth near 10 Re (Figure 5); how this connects to the SWD asymmetry is unclear. Future work evaluating SWD and FPI data in the context of IMF direction changes, hot electron enhancements and other parameters could provide more clarity regarding this asymmetry (Wang et al., 2015; Kiehas et al., 2018).

Appendix A Methods

A1 DSP SWD Validation

A TDS counter was implemented in software for this validation. It operates on the principle of minimizing the maximum electric field difference between candidate solitary structures and a pseudo-sinusoidal bipolar function. Once TDS are fit, their time-series data are removed from the remaining data and fit parameters recorded. Fitting parameters include the peak-to-peak width, amplitudes of both peaks, residuals of real data against the fit, and the predicted center time of the ESW.

The ground algorithm takes as input 65 kS/s electric field data interpolated from 8192 S/s burst data collected across spin plane probes V1-V2. It identifies bipolar solitary wave structures top-down by searching for the largest time-domain structure by peak amplitude. After locating the maximum absolute electric field value, the algorithm attempts to identify the structure's polarity by searching within a fixed number of samples of that absolute maximum for a corresponding local minimum or maximum. The algorithm then fits a modified sine wave to the structure's position, average peak-to-peak amplitude, and peak-to-peak spacing, interpolates the fitted data to align with the DCE data, records the fit parameters, then subtracts the fitted structure from the data.

The prototypical bipolar ESW signal used for validation has an amplitude of 1; peak-to-peak value of 2; and resolution of 122 sample points. The first peak is positive, and the second is negative; we refer to this polarity as a positive ESW. In the fitting process, it is centered on the ESW within 1 sample point and scaled horizontally until the x-index of each peak is within 1 sample point of the x-index of the corresponding recorded peak. To match the sample rate of EDP data, this horizontal fit is interpolated onto the recorded time range. The horizontal fit is subsequently scaled vertically on either side of the zero-crossing to match the amplitude of each peak.

An error parameter is calculated by dividing the sum of the absolute values of the subtracted sequence by the sum of the absolute values of the original sequence. If this pseudo-RMS is less than 0.2, a value manually tuned to the calibration data sequence, the fit is considered successful and the structure is counted. Otherwise, the fit is rejected. Any non-bipolar signal (like a single peak from dust impact, or a nearly continuous whistler wave) would be rejected due to its lack of similarity to the prototypical ESW signal.

In either case, the data series from the beginning to the end of that particular TDS is set to 0. The time duration of data zeroed out per structure is limited to at most 1.5 ms for structures below 50 mV/m and increases stepwise to 3.5 ms for structures larger than 100 mV/m. This conservative upper limit was set according to the assumption that structure width scales linearly with amplitude. The typical amount of time-series data removed was three times as long as the distance between the two detected peaks.

The fitting and zeroing process repeats until the maximum amplitude across the entire modified data sequence falls below a certain threshold; at that point, the algorithm writes all recorded parameters and success/rejection values. The amplitude threshold set for this work was 3 mV/m. At and above this value, the algorithm was able to terminate; with the threshold set lower, e.g. between 0.5 and 1.5 mV/m, the algorithm produced greater than 90% failed fits near the threshold. Since the lowest SWD bin within this limit is Bin 2 (3-12 mV/m), Bin 1 (0.5-3 mV/m) was excluded. More sophisticated algorithms could improve on this lower limit.

As the ground TDS detection algorithm ignores any time segments already analyzed, it is incapable of detecting solitary waves with more than 10-20% overlap. When simulated e-parallel data (with ESWs placed with uniformly random distributions and amplitudes) is supplied as an input, the ground TDS counter is able to detect 75% of all artificial ESW placed within the data, corresponding to a 25% false negative rate. Since the SWD is only able to count a single TDS within each of its sampling windows, we expect that a similar limitation will be present.

As for false positives, the ground TDS detection algorithm only examines a signal if its maximum amplitude exceeds that of all other signals in the same time series. The MMS SWD algorithm false positive rate, by comparison, is dependent on the density of non-ESW signals; it will nearly always trigger on a continuous wave provided the wave's frequency is near 1-2 kHz. In other words, the SWD has continuous false positives in certain locations, e.g. the bow shock, where the electric field is constantly changing.

A2 Map Generation

Maps were generated using binning (Oliphant, 2006; Van Der Walt et al., 2011; Hunter, 2007). The continuous nature of the SWD enables continuous, full-orbit mapping data from DSP activation (Ergun et al., 2016). Maps were generated using DSP SWD, geocentric magnetic coordinate ephemeris and FPI data collected from 2015-08 to 2020-03. 3D spatial maps were flattened into 2-dimensional XY-plane maps prior to statistical analysis; in this manner, dwell times in each bin were accurately represented. Maps are rendered with the North pole (GSE +Z) pointing out of the page. Blank (white) pixels represent spatial bins where none of the spacecraft recorded data.

Acknowledgments

This work was supported by NASA's MMS mission. All MMS data used for this research was supplied by the MMS Science Data Center hosted by the Laboratory for Atmospheric and Space Physics and accessible at `https://lasp.colorado.edu/mms/sdc/public/`. MMS data is also publicly accessible at the Space Physics Data Facility at the NASA Goddard Space Flight Center (`https://spdf.gsfc.nasa.gov/pub/data/mms/`). E. Grimes and the SPEDAS coauthors are thanked for their correspondence.

References

Andersson, L., Ergun, R. E., Newman, D. L., McFadden, J. P., Carlson, C. W., & Su, Y.-J. (2002). Characteristics of parallel electric fields in the downward current region of the aurora. *Physics of Plasmas*, *9*(8), 3600-3609. Retrieved from `https://doi.org/10.1063/1.1490134` doi: 10.1063/1.1490134

Cattell, C., Crumley, J., Dombeck, J., Wygant, J., & Mozer, F. S. (2002). Polar observations of solitary waves at the earth's magnetopause. *Geophysical Research Letters*, *29*(5), 9-1-9-4. Retrieved from `https://agupubs.onlinelibrary.wiley.com/doi/abs/10.1029/2001GL014046` doi: 10.1029/2001GL014046

Ergun, R. E., Andersson, L., Main, D. S., Su, Y.-J., Carlson, C. W., McFadden, J. P., & Mozer, F. S. (2002). Parallel electric fields in the upward current region of the aurora: Indirect and direct observations. *Physics of Plasmas*, *9*(9), 3685-3694. Retrieved from https://doi.org/10.1063/1.1499120 doi: 10.1063/1.1499120

Ergun, R. E., Carlson, C. W., McFadden, J. P., Mozer, F. S., Delory, G. T., Peria, W., ... Kistler, L. (1998). Fast satellite wave observations in the akr source region. *Geophysical Research Letters*, *25*(12), 2061-2064. Retrieved from https://agupubs.onlinelibrary.wiley.com/doi/abs/10.1029/98GL00570 doi: 10.1029/98GL00570

Ergun, R. E., Goodrich, K. A., Stawarz, J. E., Andersson, L., & Angelopoulos, V. (2015). Large-amplitude electric fields associated with bursty bulk flow braking in the earth's plasma sheet. *Journal of Geophysical Research: Space Physics*, *120*(3), 1832-1844. Retrieved from https://agupubs.onlinelibrary.wiley.com/doi/abs/10.1002/2014JA020165 doi: 10.1002/2014JA020165

Ergun, R. E., Tucker, S., Westfall, J., Goodrich, K. A., Malaspina, D. M., Summers, D., ... Cully, C. M. (2016, Mar). The axial double probe and fields signal processing for the mms mission. *Space Science Reviews*, *199*, 167-188. Retrieved from https://doi.org/10.1007/s11214-014-0115-x doi: 10.1007/s11214-014-0115-x

Goodrich, K. A., Ergun, R., Schwartz, S. J., Wilson III, L. B., Johlander, A., Newman, D., ... Giles, B. (2019). Impulsively reflected ions: A plausible mechanism for ion acoustic wave growth in collisionless shocks. *Journal of Geophysical Research: Space Physics*, *124*(3), 1855-1865. Retrieved from https://agupubs.onlinelibrary.wiley.com/doi/abs/10.1029/2018JA026436 doi: 10.1029/2018JA026436

Goodrich, K. A., Ergun, R., Schwartz, S. J., Wilson III, L. B., Newman, D., Wilder, F. D., ... Andersson, L. (2018). Mms observations of electrostatic waves in an oblique shock crossing. *Journal of Geophysical Research: Space Physics*, *123*(11), 9430-9442. Retrieved from https://agupubs.onlinelibrary.wiley.com/doi/abs/10.1029/2018JA025830 doi: 10.1029/2018JA025830

Graham, D. B., Khotyaintsev, Y. V., Vaivads, A., & Andr, M. (2016). Electrostatic solitary waves and electrostatic waves at the magnetopause. *Journal of Geophysical Research: Space Physics*, *121*(4), 3069-3092. Retrieved from https://agupubs.onlinelibrary.wiley.com/doi/abs/10.1002/2015JA021527 doi: 10.1002/2015JA021527

Holmes, J. C., Ergun, R. E., Newman, D. L., Ahmadi, N., Andersson, L., Le Contel, O., ... Burch, J. L. (2018). Electron phase-space holes in three dimensions: Multispacecraft observations by magnetospheric multiscale. *Journal of Geophysical Research: Space Physics*, *123*(12), 9963-9978. Retrieved from https://agupubs.onlinelibrary.wiley.com/doi/abs/10.1029/2018JA025750 doi: 10.1029/2018JA025750

Hunter, J. D. (2007). Matplotlib: A 2d graphics environment. *Computing in Science & Engineering*, *9*(3), 90–95. doi: 10.1109/MCSE.2007.55

Kiehas, S. A., Runov, A., Angelopolos, V., Hietala, H., & Korovinksiy, D. (2018). Magnetotail fast flow occurrence rate and dawn-dusk asymmetry at xgsm 60 re. *Journal of Geophysical Research: Space Physics*, *123*(3), 1767-1778. Retrieved from https://agupubs.onlinelibrary.wiley.com/doi/abs/10.1002/2017JA024776 doi: 10.1002/2017JA024776

Kojima, H., Matsumoto, H., & Omura, Y. (1999). Electrostatic solitary waves observed in the geomagnetic tail and other regions. *Advances in Space Research*, *23*(10), 1689 - 1697. Retrieved from http://www.sciencedirect.com/science/article/pii/S0273117799003774 doi: https://doi.org/10.1016/

S0273-1177(99)00377-4

Le Contel, O., Nakamura, R., Breuillard, H., Argall, M. R., Graham, D. B., & Fischer, A. N., D. ... Jaynes. (2017). Lower hybrid drift waves and electromagnetic electron space-phase holes associated with dipolarization fronts and field-aligned currents observed by the magnetospheric multiscale mission during a substorm. *Journal of Geophysical Research: Space Physics*, *122*, 12236-12257. doi: 10.1002/2017JA024550

Lindqvist, P.-A., Olsson, T. R. B., G., King, B., Granoff, M., Rau, D., Needell, G., ... Tucker, S. (2016, Mar). The spin-plane double probe electric field instrument for mms. *Space Science Reviews*, *199*, 137.

Main, D. S., Newman, D. L., & Ergun, R. E. (2006, Nov). Double layers and ion phase-space holes in the auroral upward-current region. *Phys. Rev. Lett.*, *97*, 185001. Retrieved from `https://link.aps.org/doi/10.1103/PhysRevLett.97.185001` doi: 10.1103/PhysRevLett.97.185001

Malaspina, D. M., Newman, D. L., Willson III, L. B., Goetz, K., Kellogg, P. J., & Kerstin, K. (2013). Electrostatic solitary waves in the solar wind: Evidence for instability at solar wind current sheets. *Journal of Geophysical Research: Space Physics*, *118*(2), 591-599. Retrieved from `https://agupubs.onlinelibrary.wiley.com/doi/abs/10.1002/jgra.50102` doi: 10.1002/jgra.50102

Mangeney, A., Salem, C., Lacombe, C., Bougeret, J., Perche, C., Manning, R., ... Bosqued, J. (1999, March). Wind observations of coherent electrostatic waves in the solar wind. *Annales Geophysicae*, *17*(3), 307–320. doi: 10.1007/s00585-999-0307-y

Matsumoto, H., Kojima, H., Miyatake, T., Omura, Y., Okada, M., Nagano, I., & Tsutsui, M. (1994). Electrostatic solitary waves (esw) in the magnetotail: Ben wave forms observed by geotail. *Geophysical Research Letters*, *21*(25), 2915-2918. Retrieved from `https://agupubs.onlinelibrary.wiley.com/doi/abs/10.1029/94GL01284` doi: 10.1029/94GL01284

McPherron, R. L., Hsu, T.-S., Kissinger, J., Chu, X., & Angelopoulos, V. (2011). Characteristics of plasma flows at the inner edge of the plasma sheet. *Journal of Geophysical Research: Space Physics*, *116*(A5). Retrieved from `https://agupubs.onlinelibrary.wiley.com/doi/abs/10.1029/2010JA015923` doi: 10.1029/2010JA015923

Mozer, F., Bale, S., Bonnell, J., Chaston, C., Roth, I., & Wygant, J. (2013). Megavolt parallel potentials arising from double-layer streams in the earth's outer radiation belt. *Phys Rev Lett.*, *111*(235002). doi: 10.1103/PhysRevLett.111.2350021

Mozer, F. S., Agapitov, O. A., Artemyev, A., Burch, J. L., Ergun, R. E., Giles, B. L., ... Vasko, I. (2016, Apr). Magnetospheric multiscale satellite observations of parallel electron acceleration in magnetic field reconnection by fermi reflection from time domain structures. *Phys. Rev. Lett.*, *116*, 145101. Retrieved from `https://link.aps.org/doi/10.1103/PhysRevLett.116.145101` doi: 10.1103/PhysRevLett.116.145101

Muschietti, L., Ergun, R. E., Roth, I., & Carlson, C. W. (1999). Phase-space electron holes along magnetic field lines. *Geophysical Research Letters*, *26*(8), 1093-1096. Retrieved from `https://agupubs.onlinelibrary.wiley.com/doi/abs/10.1029/1999GL900207` doi: 10.1029/1999GL900207

Neugebauer, M., & Snyder, C. (1962). The mission of mariner ii: Preliminary observations. *Science*, *138*, 1095-1097. Retrieved from `https://science.sciencemag.org/content/138/3545/1095.2` doi: 10.1126/science.138.3545.1095-a

Oliphant, T. E. (2006). *A guide to numpy* (Vol. 1). Trelgol Publishing USA.

Omura, Y., Kojima, H., Miki, N., Mukai, T., Matsumoto, H., & Anderson, R. (1999). Electrostatic solitary waves carried by diffused electron beams observed by the

geotail spacecraft. *Journal of Geophysical Research: Space Physics*, *104*(A7), 14627-14637. Retrieved from https://agupubs.onlinelibrary.wiley.com/doi/abs/10.1029/1999JA900103 doi: 10.1029/1999JA900103

Pollock, J., Moore, T., Jacques, A., Burch, J., & et al. (2016). Fast plasma investigation for magnetospheric multiscale. *Space Science Reviews*. Retrieved from https://link.springer.com/article/10.1007/s11214-016-0245-4

Sergeev, V., Angelopoulos, V., Apatenkov, S., Bonnell, J., Ergun, R., Nakamura, R., ... Runov, A. (2009). Kinetic structure of the sharp injection/dipolarization front in the flow-braking region. *Geophysical Research Letters*, *36*(21). Retrieved from https://agupubs.onlinelibrary.wiley.com/doi/abs/10.1029/2009GL040658 doi: 10.1029/2009GL040658

Stawarz, J. E., Ergun, R. E., & Goodrich, K. A. (2015). Generation of high-frequency electric field activity by turbulence in the earth's magnetotail. *Journal of Geophysical Research: Space Physics*, *120*(3), 1845-1866. Retrieved from https://agupubs.onlinelibrary.wiley.com/doi/abs/10.1002/2014JA020166 doi: 10.1002/2014JA020166

Temerin, M., Cerny, K., Lotko, W., & Mozer, F. S. (1982, Apr). Observations of double layers and solitary waves in the auroral plasma. *Phys. Rev. Lett.*, *48*, 1175–1179. Retrieved from https://link.aps.org/doi/10.1103/PhysRevLett.48.1175 doi: 10.1103/PhysRevLett.48.1175

Van Der Walt, S., Colbert, S. C., & Varoquaux, G. (2011). The numpy array: a structure for efficient numerical computation. *Computing in Science & Engineering*, *13*(2), 22.

Vasko, I. Y., Agapitov, O. V., Mozer, F. S., Artemyev, A. V., Drake, J. F., & Kuzichev, I. V. (2017). Electron holes in the outer radiation belt: Characteristics and their role in electron energization. *Journal of Geophysical Research: Space Physics*, *122*(1), 120-135. Retrieved from https://agupubs.onlinelibrary.wiley.com/doi/abs/10.1002/2016JA023083 doi: 10.1002/2016JA023083

Wang, C.-P., Xing, X., Nakamura, T. K. M., & Lyons, L. R. (2015). Dawn-dusk asymmetry in bursty hot electron enhancements in the midtail magnetosheath. *Journal of Geophysical Research: Space Physics*, *120*(9), 7228-7239. Retrieved from https://agupubs.onlinelibrary.wiley.com/doi/abs/10.1002/2015JA021522 doi: 10.1002/2015JA021522

Wilder, F. D., Ergun, R. E., Goodrich, K. A., Goldman, M. V., Newman, D. L., Malaspina, D. M., ... Holmes, J. C. (2016). Observations of whistler mode waves with nonlinear parallel electric fields near the dayside magnetic reconnection separatrix by the magnetospheric multiscale mission. *Geophysical Research Letters*, *43*(12), 5909-5917. Retrieved from https://agupubs.onlinelibrary.wiley.com/doi/abs/10.1002/2016GL069473 doi: 10.1002/2016GL069473

Zhang, L. Q., Baumjohann, W., Khotyaintsev, Y. V., Burch, J. L., Webster, J., Wang, J. Y., ... Zhang, C. Y. (2020). Bbf deceleration down-tail of x ¡ 15 re from mms observation. *Journal of Geophysical Research: Space Physics*, *125*(2), e2019JA026837. Retrieved from https://agupubs.onlinelibrary.wiley.com/doi/abs/10.1029/2019JA026837 (e2019JA026837 2019JA026837) doi: 10.1029/2019JA026837

Figure 1.

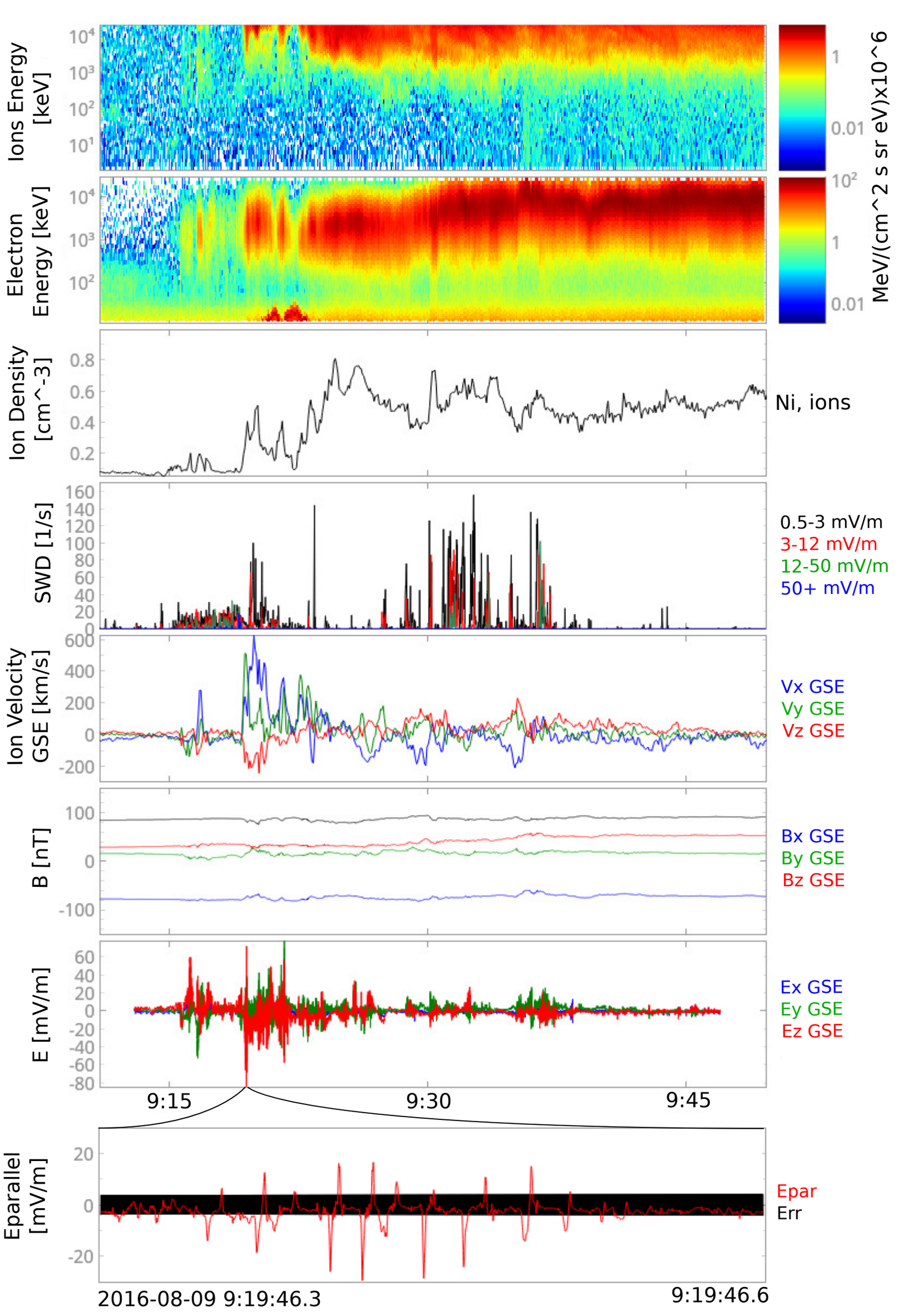
Ions Energy [keV]
Electron Energy [keV]
MeV/(cm^2 s sr eV)x10^6
Ion Density [cm^-3]
Ni, ions
SWD [1/s]
0.5-3 mV/m
3-12 mV/m
12-50 mV/m
50+ mV/m
Ion Velocity GSE [km/s]
Vx GSE
Vy GSE
Vz GSE
B [nT]
Bx GSE
By GSE
Bz GSE
E [mV/m]
Ex GSE
Ey GSE
Ez GSE
9:15
9:30
9:45
Eparallel [mV/m]
Epar
Err
2016-08-09 9:19:46.3
9:19:46.6

Figure 2A.

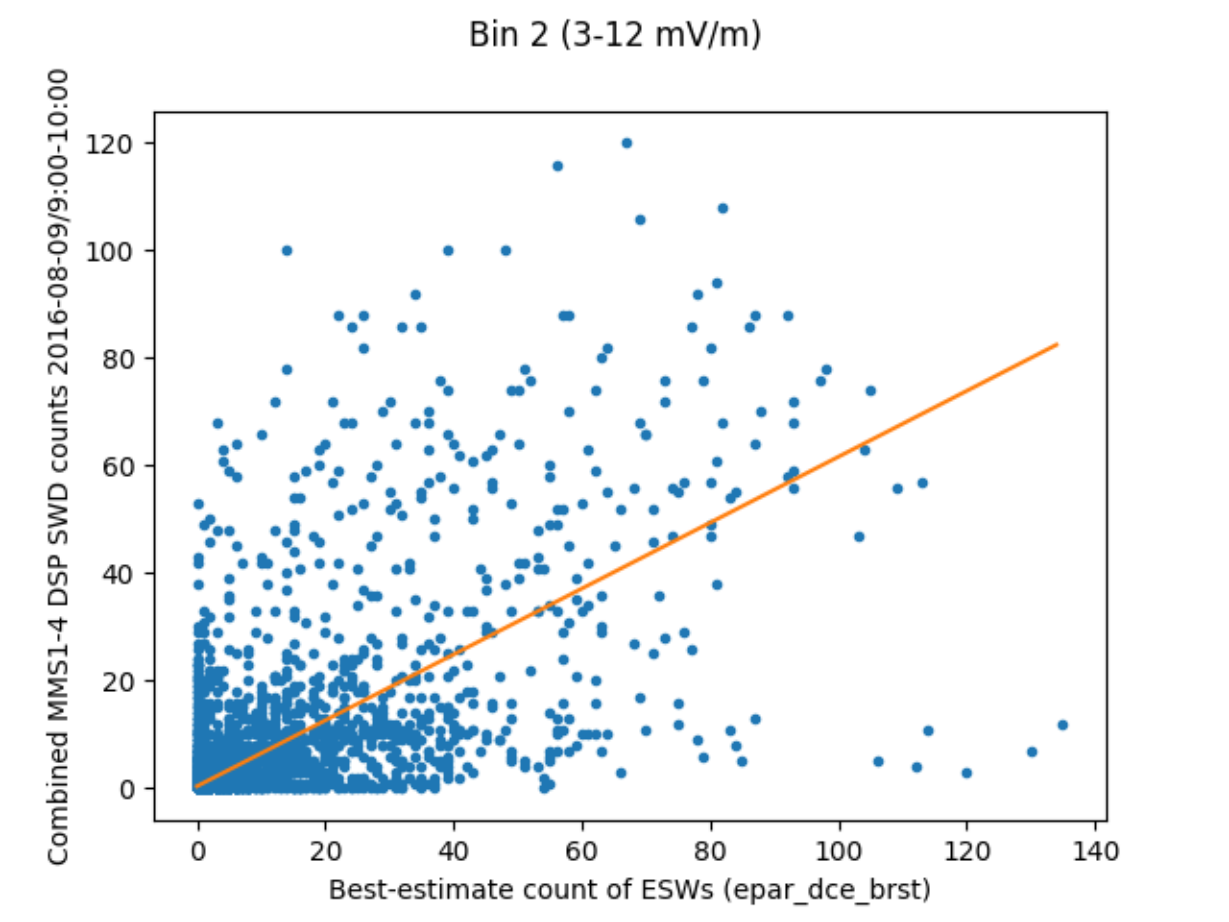
Bin 2 (3-12 mV/m)
Combined MMS1-4 DSP SWD counts 2016-08-09/9:00-10:00
Best-estimate count of ESWs (epar_dce_brst)
0
20
40
60
80
100
120
140

Figure 2B.

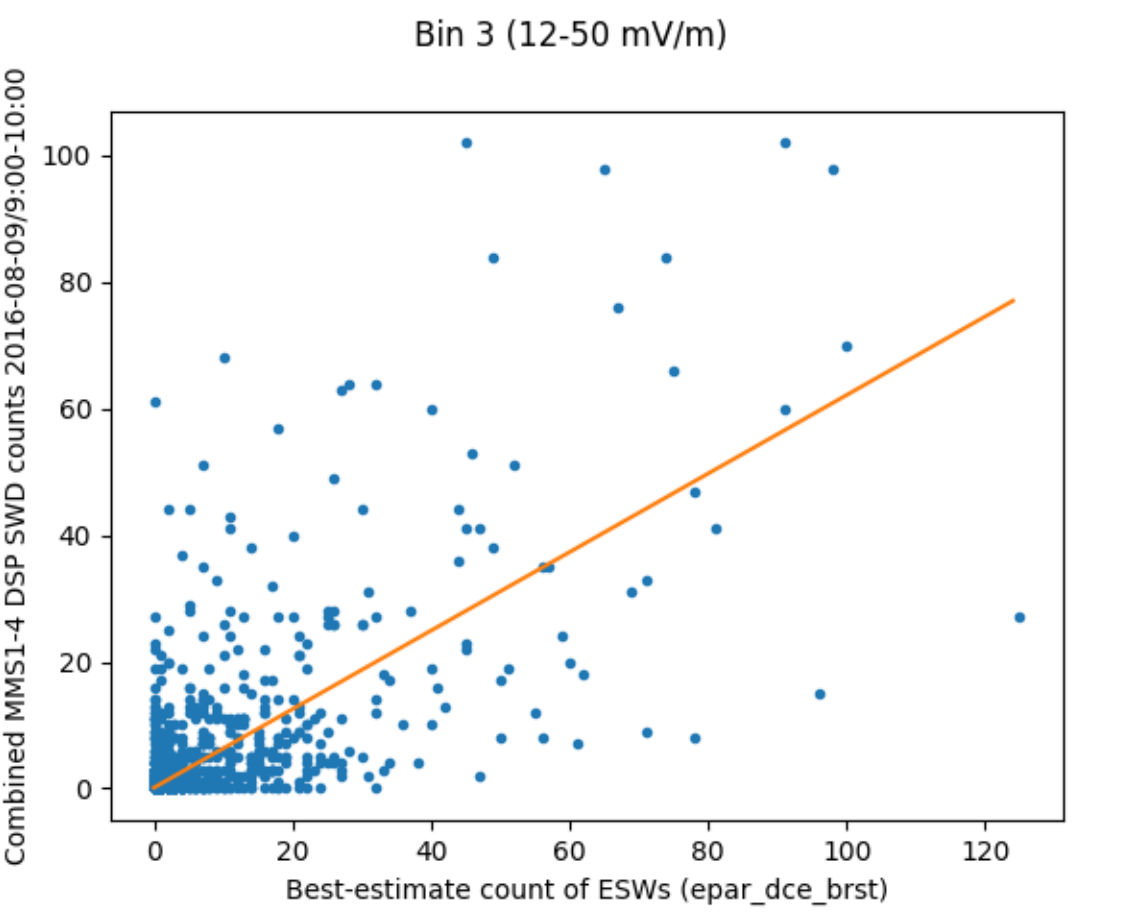
Bin 3 (12-50 mV/m)
Combined MMS1-4 DSP SWD counts 2016-08-09/9:00-10:00
Best-estimate count of ESWs (epar_dce_brst)
0
20
40
60
80
100
120

Figure 2C.

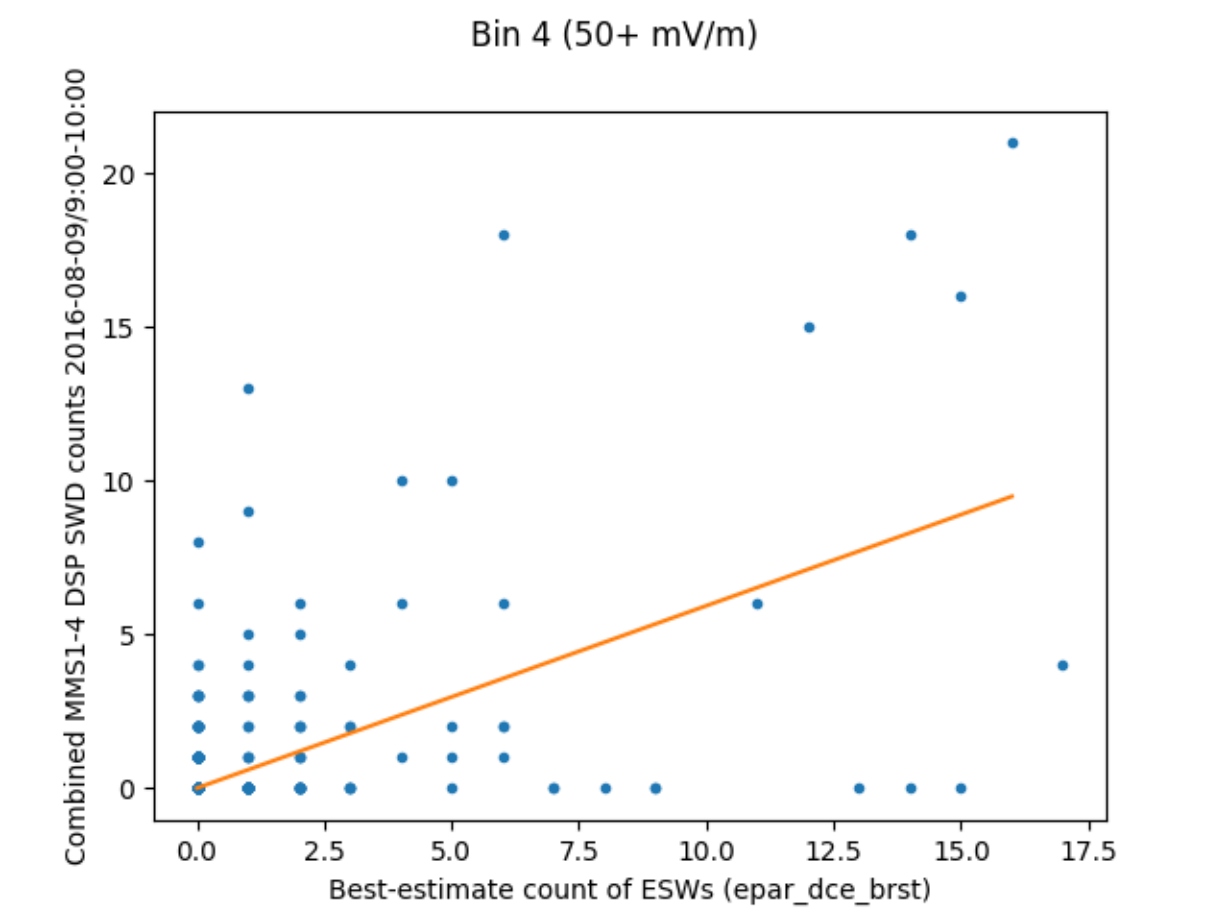
Bin 4 (50+ mV/m)
Combined MMS1-4 DSP SWD counts 2016-08-09/9:00-10:00
Best-estimate count of ESWs (epar_dce_brst)
0
5
10
15
20
0.0
2.5
5.0
7.5
10.0
12.5
15.0
17.5

Figure 3A.

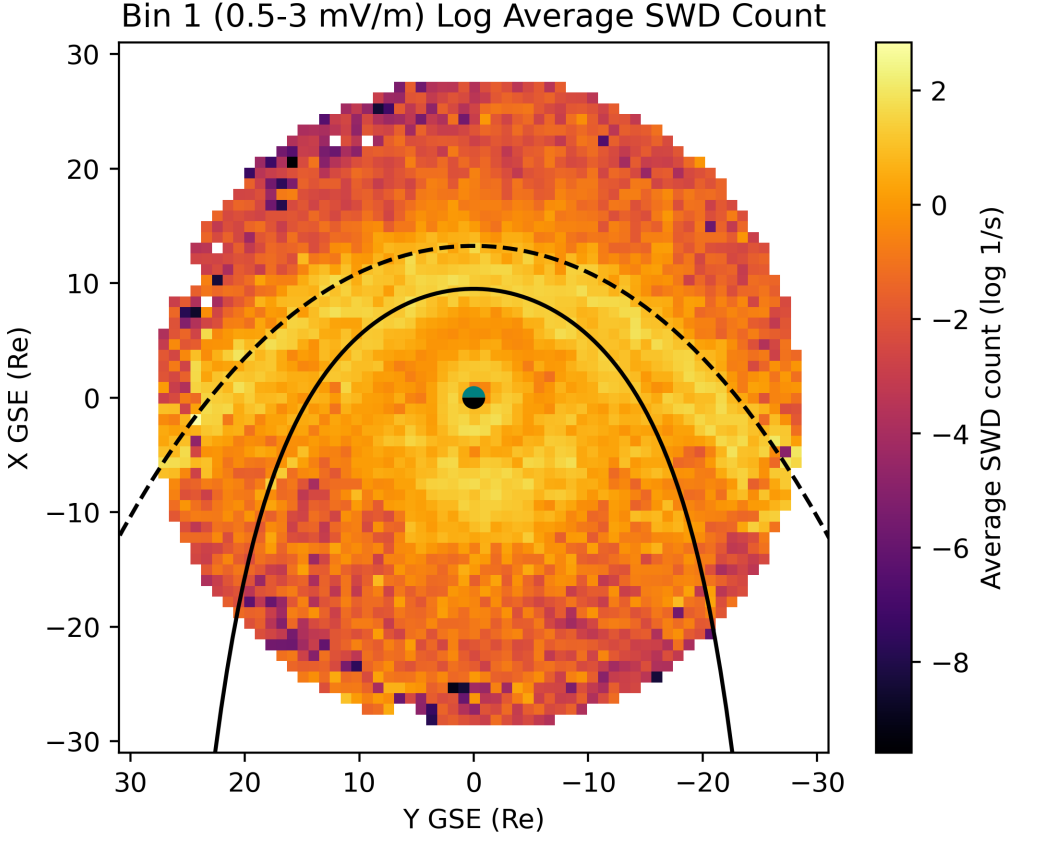
Bin 1 (0.5-3 mV/m) Log Average SWD Count
X GSE (Re)
Y GSE (Re)
Average SWD count (log 1/s)
30
20
10
0
−10
−20
−30
2
0
−2
−4
−6
−8

Figure 3B.

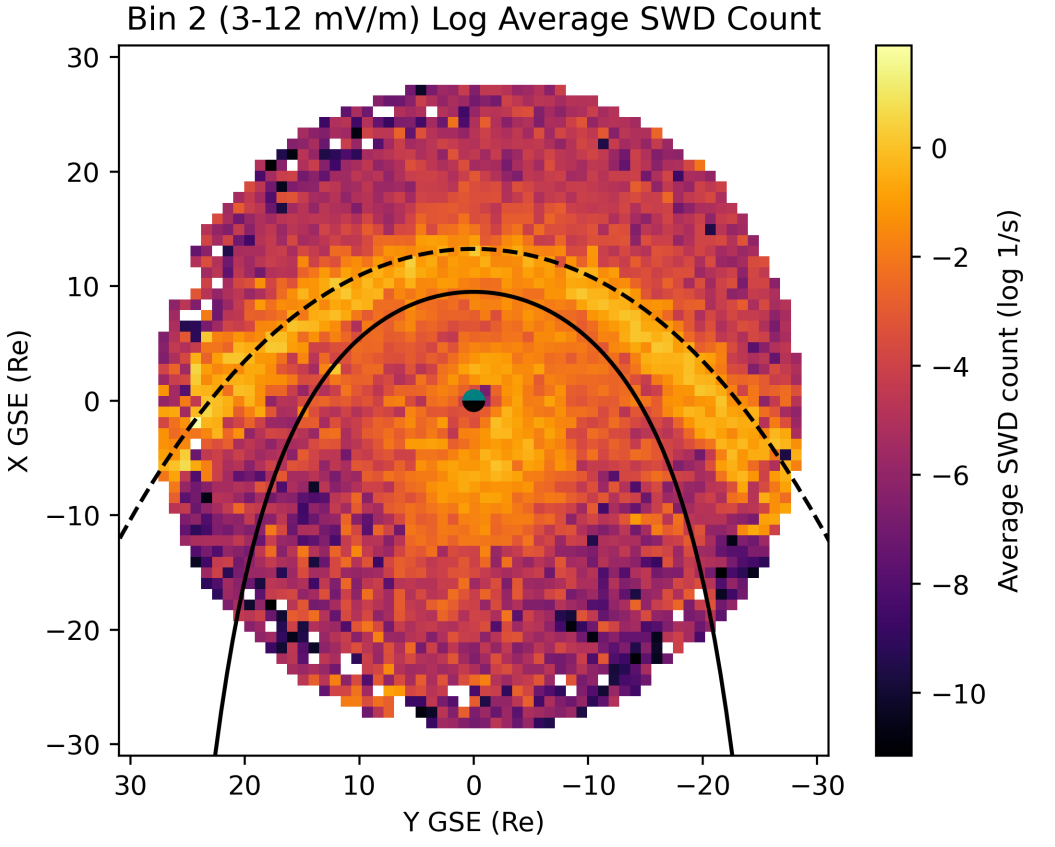
Bin 2 (3-12 mV/m) Log Average SWD Count
X GSE (Re)
Y GSE (Re)
Average SWD count (log 1/s)
30
20
10
0
−10
−20
−30
0
−2
−4
−6
−8
−10

Figure 4A.

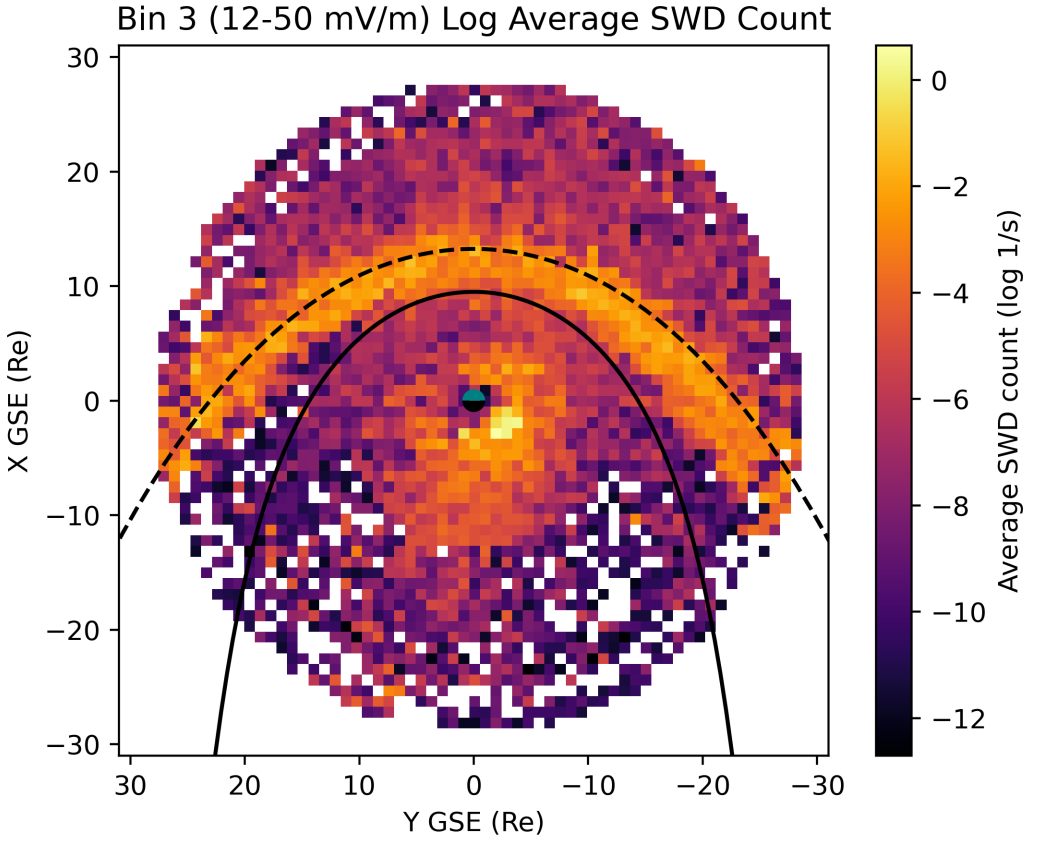
Bin 3 (12-50 mV/m) Log Average SWD Count
X GSE (Re)
Y GSE (Re)
Average SWD count (log 1/s)
30
20
10
0
−10
−20
−30
0
−2
−4
−6
−8
−10
−12

Figure 4B.

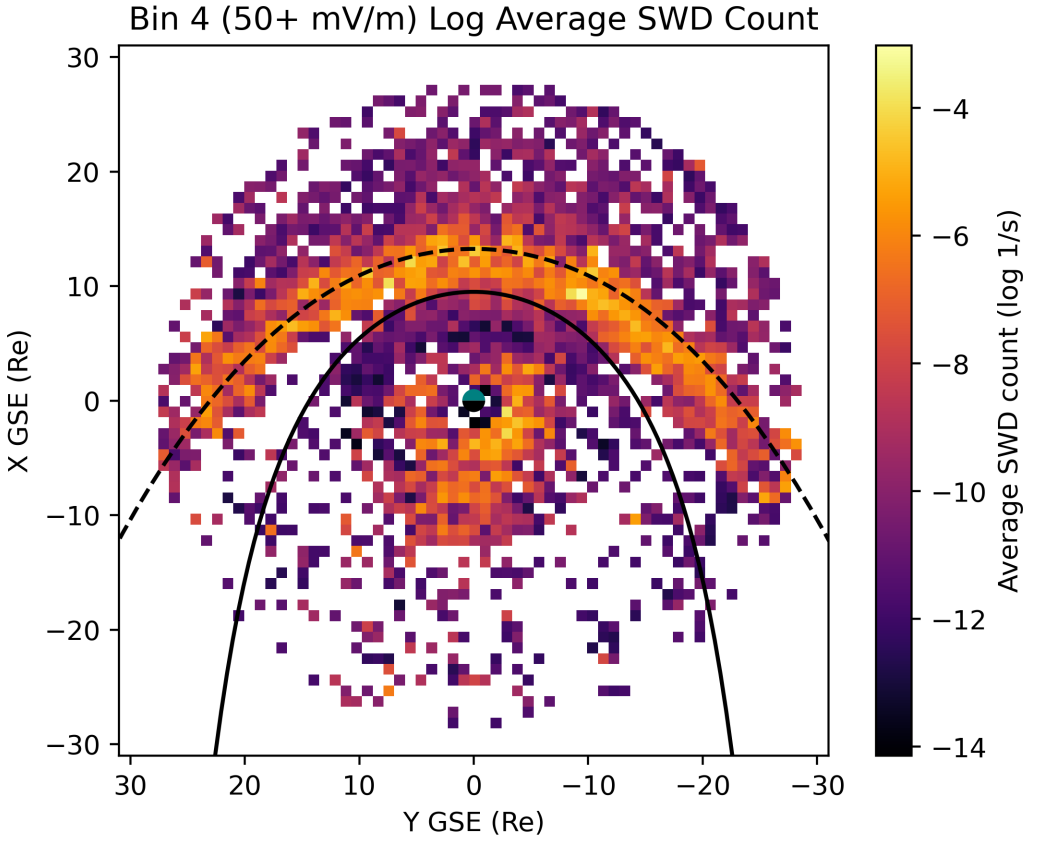
Bin 4 (50+ mV/m) Log Average SWD Count
X GSE (Re)
Y GSE (Re)
Average SWD count (log 1/s)
30
20
10
0
−10
−20
−30
−4
−6
−8
−10
−12
−14

Figure 5A.

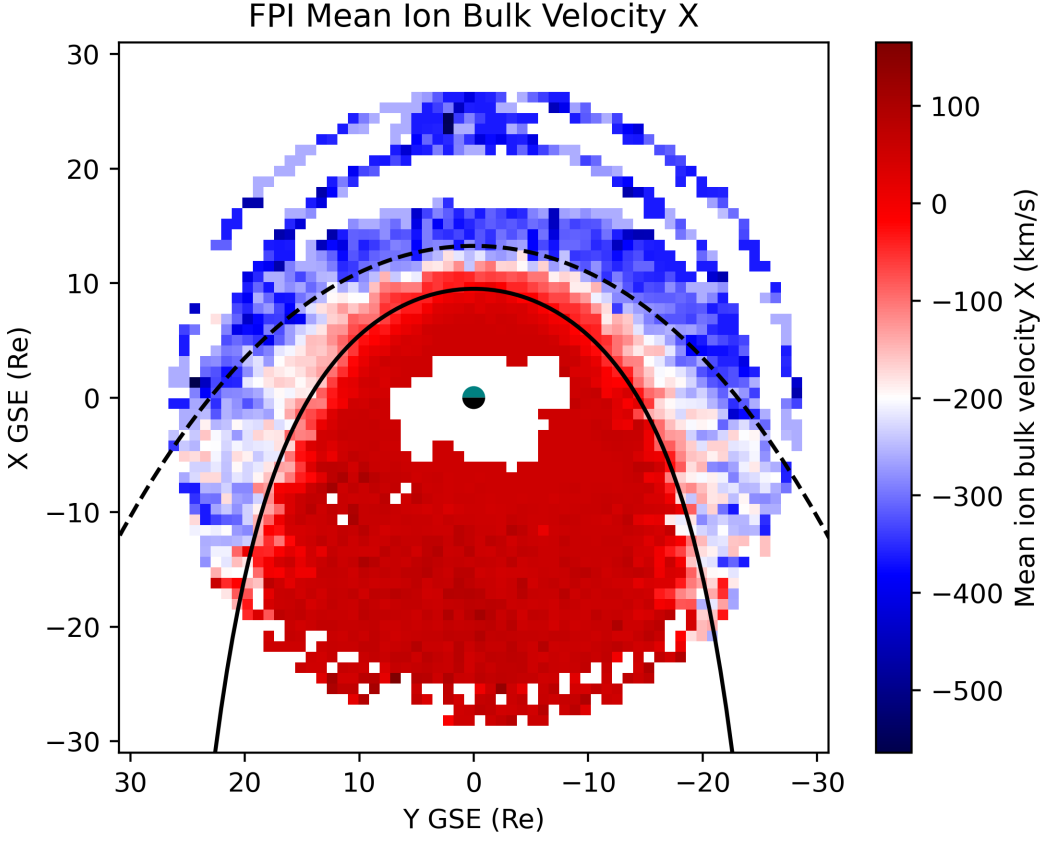
FPI Mean Ion Bulk Velocity X
X GSE (Re)
Y GSE (Re)
Mean ion bulk velocity X (km/s)
30
20
10
0
−10
−20
−30
100
0
−100
−200
−300
−400
−500

Figure 5B.

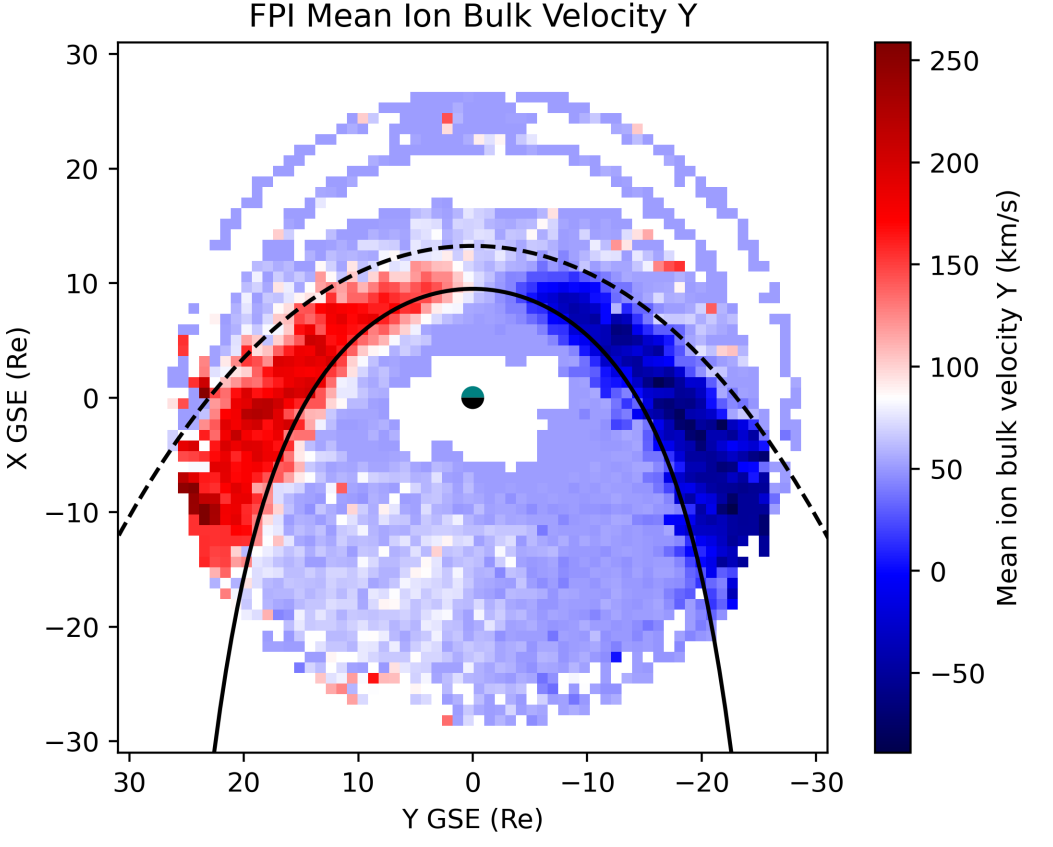
FPI Mean Ion Bulk Velocity Y
X GSE (Re)
Y GSE (Re)
Mean ion bulk velocity Y (km/s)
30
20
10
0
−10
−20
−30
250
200
150
100
50
0
−50

Figure 6A.

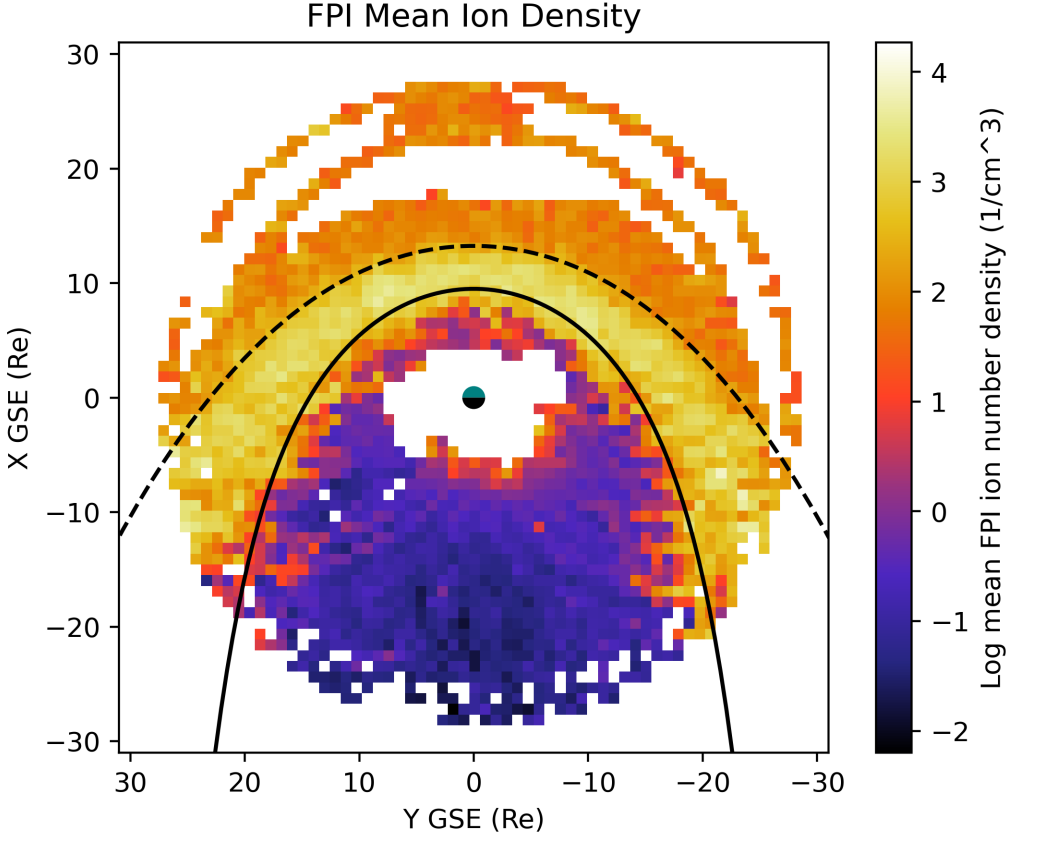
FPI Mean Ion Density
X GSE (Re)
Y GSE (Re)
Log mean FPI ion number density (1/cm^3)
30
20
10
0
−10
−20
−30
4
3
2
1
0
−1
−2

Figure 6B.

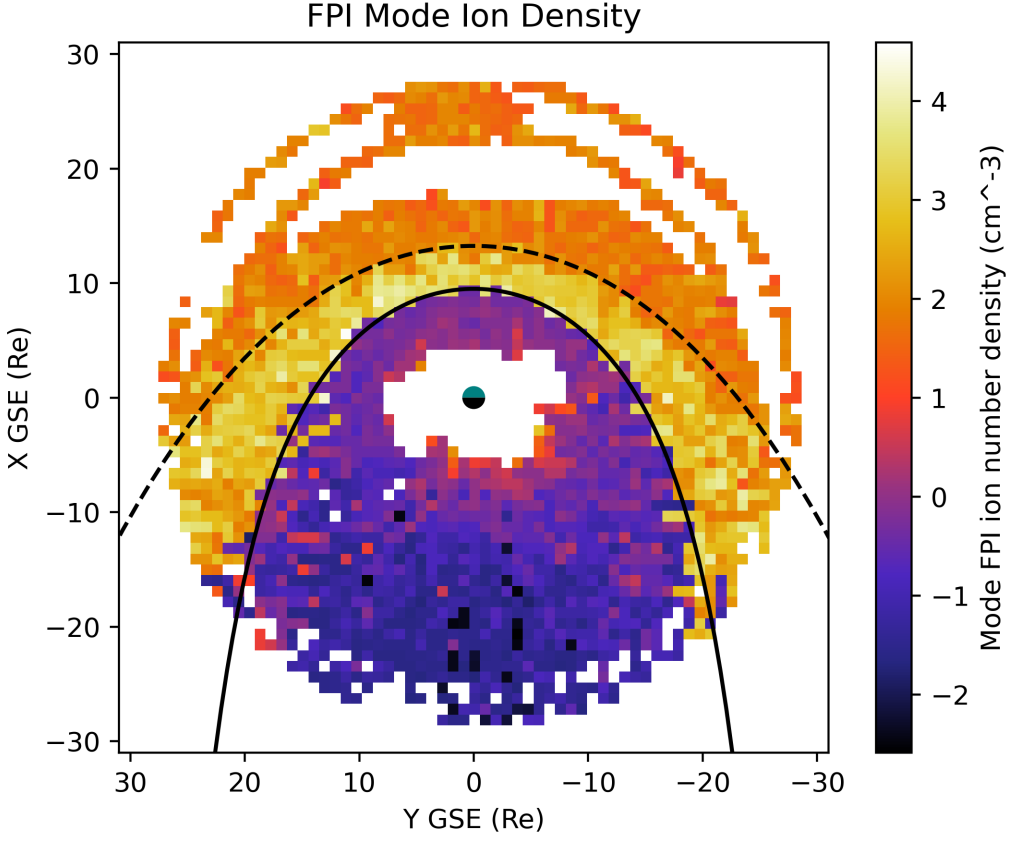
FPI Mode Ion Density
X GSE (Re)
Y GSE (Re)
Mode FPI ion number density (cm^-3)
30
20
10
0
−10
−20
−30
4
3
2
1
0
−1
−2